Research Article Vol. 5, No. 1 / January 2018 / Optica 44

High-performance flexible waveguide-integrated photodetectors

Lan Li,[1,4,†] Hongtao Lin,[1,†] Yizhong Huang,[1] Ren-Jye Shiue,[2] Anupama Yadav,[3] Junying Li,[1] Jerome Michon,[1] Dirk Englund,[2] Kathleen Richardson,[3] Tian Gu,[1] and Juejun Hu[1,*]

[1]Department of Materials Science & Engineering, Massachusetts Institute of Technology, Cambridge, Massachusetts 02139, USA
[2]Department of Electrical Engineering and Computer Science, Massachusetts Institute of Technology, Cambridge, Massachusetts 02139, USA
[3]The College of Optics & Photonics, University of Central Florida, Orlando, Florida 32816, USA
[4]e-mail: lanli1@mit.edu
*Corresponding author: hujuejun@mit.edu

Received 23 October 2017; revised 3 December 2017; accepted 8 December 2017 (Doc. ID 309771); published 11 January 2018

Mechanically flexible photonic devices are essential building blocks for novel bio-integrated optoelectronic systems, wearable sensors, and flexible consumer electronics. Here we describe the design and experimental demonstration of high-performance flexible semiconductor nanomembrane photodetectors integrated with single-mode chalcogenide glass waveguides. Through a combination of a waveguide-integrated architecture to enhance light–matter interactions and mechanical engineering of multilayer configurations to suppress strains, the detector devices exhibit record optical and mechanical performance. The devices feature a noise equivalent power as low as 0.02 pW · Hz$^{1/2}$, a linear dynamic range exceeding 70 dB, and a 3-dB bandwidth of 1.4 GHz, all measured at 1530 nm wavelength. The devices withstand 1000 bending cycles at a submillimeter radius without degradation in their optoelectronic responses. These metrics represent significant improvements over state-of-the-art flexible photodetectors.

OCIS codes: (230.3120) Integrated optics devices; (230.5160) Photodetectors; (130.2755) Glass waveguides; (130.5990) Semiconductors.

https://doi.org/10.1364/OPTICA.5.000044

1. INTRODUCTION

In recent years, emerging applications of mechanically flexible photonic systems have flourished in fields encompassing short-reach data communications [1–3], stress monitoring [4–6], wearable devices [7–9], implantable sensors [10–12], optical tuning [13–15], and roll-to-roll photonic manufacturing [16–19]. Flexible photodetectors, an essential component for such systems, have thus received significant developmental attention and research efforts in the scientific community. To meet the demands of the aforementioned applications, a successful flexible photodetector design necessarily mandates both mechanical ruggedness and superior optical performance such as high signal-to-noise ratio (SNR) and fast response. To date, flexible photodetector devices have been implemented based on several material platforms, including organic polymers [20–23], nanowires or nanotubes [24–30], 2D materials [31–34], perovskites [35–38], and semiconductor nanomembranes (NMs) [39–43]. Supplement 1 (Table S1) highlights state-of-the-art flexible photodetector devices fabricated from these material systems. Unfortunately, few material platforms can simultaneously meet the mechanical and optical performance requirements of robust high-performance applications. For instance, organic polymers are inherently flexible; however, their inferior electronic and thermal properties limit the stability and performance of resulting devices. On the other hand, while nanowires are mechanically compliant, efficient optical coupling into a single nanowire is challenging. Using nanowire ensembles eases device integration and optical interfacing, albeit at the expense of carrier transport characteristics. Semiconductor NMs, single crystal slices with sub-micrometer thickness that inherit the singular optoelectronic quality of their parent semiconductor materials, are particularly promising for high-performance detector fabrication. Nevertheless, NM devices realized thus far only exhibit limited mechanical flexibility with minimum bending radii no less than a few millimeters.

Here we demonstrated waveguide-integrated flexible photodetectors based on $In_{0.53}Ga_{0.47}As$ (InGaAs) NMs that boast exceptional optical performances in terms of SNR, speed, and linear range, as well as extraordinary mechanical flexibility and robustness, capable of sustaining repeated deformation at a sub-millimeter bending radius without measurable degradation. Such performances benefit from a unique combination of a single-mode waveguide-integrated configuration and a multilayer mechanical design building on the multi-neutral-axis (MNA) theory [44–46]. Compared to their free-space counterparts, waveguide-integrated detectors not only facilitate planar photonic integration, but also offer a significant performance advantage in

terms of speed and SNR [47]. In waveguide-integrated detectors, the carrier collection path and the light propagation direction are orthogonal, thereby circumventing the trade-off between bandwidth and quantum efficiency. In addition, the small detector size enabled by a single-mode waveguide coupling design is conducive to low noise operation of the device, as the most commonly encountered detector noise sources (shot noise, Johnson noise, and generation-recombination noise) all scale with the detector active volume. While waveguide-integrated flexible detectors have previously been realized, these devices operate exclusively with large-core multi-mode waveguides [48–50]. Our work represents the first demonstration of single-mode waveguide-integrated flexible detectors that fully captures the SNR and bandwidth advantages of waveguide-integrated architectures.

In optimizing the mechanical design for such structures, we applied for the first time the MNA theory to NM optoelectronic devices to confer unprecedented mechanical flexibility and ruggedness to the candidate system. In our case, the design implements a multilayer structure comprising laminae with a giant elastic modulus contrast to release strains exerted on the active detector NM, thereby eliminating deleterious effects resulting from mechanical failure of NMs during repeated bending deformation [44–46].

The following sections detail the design, fabrication, and characterization results of the device.

2. DEVICE DESIGN, FABRICATION, AND CHARACTERIZATION

The detector fabrication combines III-V die-to-wafer bonding and direct chalcogenide glass (ChG) waveguide fabrication, where the former provides high active material quality and the latter significantly simplifies the integration process by eliminating the need for a second hybrid transfer or bonding step. Figure 1(a) schematically illustrates the fabrication process flow of the waveguide-integrated metal-semiconductor-metal (MSM) photodetector. The process starts with an oxide-coated silicon wafer (Silicon Quest International) as the handler substrate. A SU-8 epoxy (Microchem SU-8 2005) film, which acts as both the under cladding and an adhesive bonding agent, was spin coated and soft baked at 95°C for 2 min. The SU-8 film was then flood exposed with a dose of 53 mJ/cm^2, half of the manufacturer prescribed value, such that the epoxy is only partially cross-linked. This step ensures that the epoxy can still reflow during the subsequent bonding step. An InP die (diced into 2 cm × 1 cm chips) with an epitaxially grown InGaAs active layer was bonded onto the Si wafer with the epi-layer facing the SU-8 epoxy using a home-built pressure loader. The detailed epi-layer sequence is listed in Supplement 1 (Table S2). The bonding process was carried out at 90°C for 20 min followed by 150°C for 20 min in a vacuum oven. The pressure loader and the sample were furnace cooled to room temperature, during which they remained in the vacuum oven to avoid cracking in the epi-layer. The InP substrate was removed by mechanical lapping followed by wet chemical etching, leaving behind a NM consisting of the InGaAs absorber and an InAlAs Schottky barrier enhancement layer, totaling about 200 nm in thickness. The NM was subsequently patterned using electron beam lithography and wet etching to define the detector mesas. Detailed processing parameters of the NM fabrication steps are summarized in Supplement 1 (Table S3). Next, metal contacts (20-nm/100-nm Ti/Au) were deposited on the NM and patterned via lift-off. Single-mode waveguides (450-nm-thick and 800-nm-wide) straddling across the detector mesas were then fabricated from thermally evaporated $Ge_{23}Sb_7S_{70}$ chalcogenide glass films using a double-layer resist lift-off process [51–53]. Lastly, a second SU-8 layer (the top cladding, Microchem SU-8 2010) was spin coated, and windows were lithographically opened in the SU-8 layer to allow probe access to the metal contacts. The entire SU-8 encapsulated structure was delaminated from the handler wafer by immersing the wafer in dilute hydrofluoric acid (5.2 wt.%) for 30 min, and finally attached to a Kapton tape (KPT-1, kaptontape.com) to complete the fabrication process.

Figure 2(a) depicts the resulting multilayer structure of the flexible detector. The Kapton tape serves both as a structural support to facilitate handling and as an integral part enabling the MNA design with its silicone–polyimide bilayer structure. The MNA theory predicts that when a low-modulus silicone adhesive layer (Young's modulus 1.5 MPa) is sandwiched between the stiff SU-8 (Young's modulus 2 GPa) and polyimide (Young's modulus 2.5 GPa) films, the soft silicone layer sustains large shear deformation and thereby effectively releases strains exerted on other laminae during bending [44]. Figure 2(b) plots the mechanical strain at the center plane of the NM as functions of the top and bottom SU-8 cladding layer thicknesses modeled using the MNA theory. The optimal designs correspond to the bolded line where the vanishing strain imparts extraordinary mechanical flexibility to the NM devices. The star symbol marks the experimentally realized device configuration where the actual SU-8 thicknesses were measured through cross-sectional SEM. Figures 2(c) and 2(d) plot the strain distribution in the fabricated device simulated using the finite element method (FEM) when it is bent to 0.8 mm radius. The simulation reveals that peak strain inside the NM is merely 0.07%, a 72-fold reduction compared to the largest strain in the entire stack. The dramatic strain suppression underlies the remarkable mechanical robustness of our device, despite the slight deviation from the ideal case due to imperfect SU-8 thickness control.

In our device, light is funneled into the detector through a single-mode ChG waveguide straddling across the NM mesa. The detector mesa length is 30 μm and the spacing between electrical contacts is 3 μm. This design simplifies the device fabrication process and leads to a high coupling efficiency with properly engineered waveguide modes. Figure 3(a) presents the optical intensity distribution in the waveguide-coupled detector structure modeled using the finite-difference time-domain (FDTD) method along the center plane of the waveguide. The material parameters used in the simulation are summarized in Supplement 1 (Table S4). The model indicates an optical absorption efficiency of 86%, where 10% of light is lost at the junction between the waveguide and the detector mesa due to scattering and reflection, and 4% of light traverses across the structure without being absorbed. To gain further insight into the coupling mechanism, we plot the optical modal profiles in the input glass waveguide [Fig. 3(b)] as well as in the detector [Figs. 3(c) and 3(d) inset]. As can be seen, the detector section (where the ChG waveguide sits on the NM) supports two guided supermodes, an even mode primarily confined in the high-index NM [Fig. 3(c)] and an odd mode that largely resides in the ChG waveguide [Fig. 3(d) inset]. Most input light is channeled into the symmetric NM supermode and strongly absorbed by the NM. This is also evident from Fig. 3(d), which shows the optical power flux (normalized to

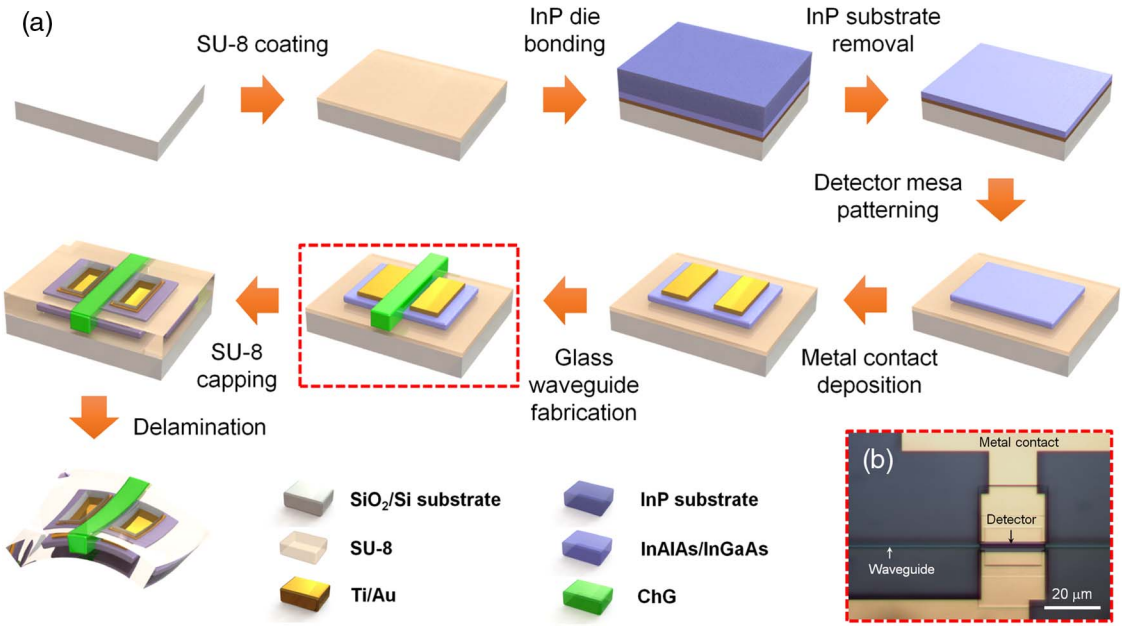

Fig. 1. (a) Schematic fabrication process flow of the flexible waveguide-integrated detector; (b) top-view optical micrograph of a detector prior to the SU-8 top cladding capping step.

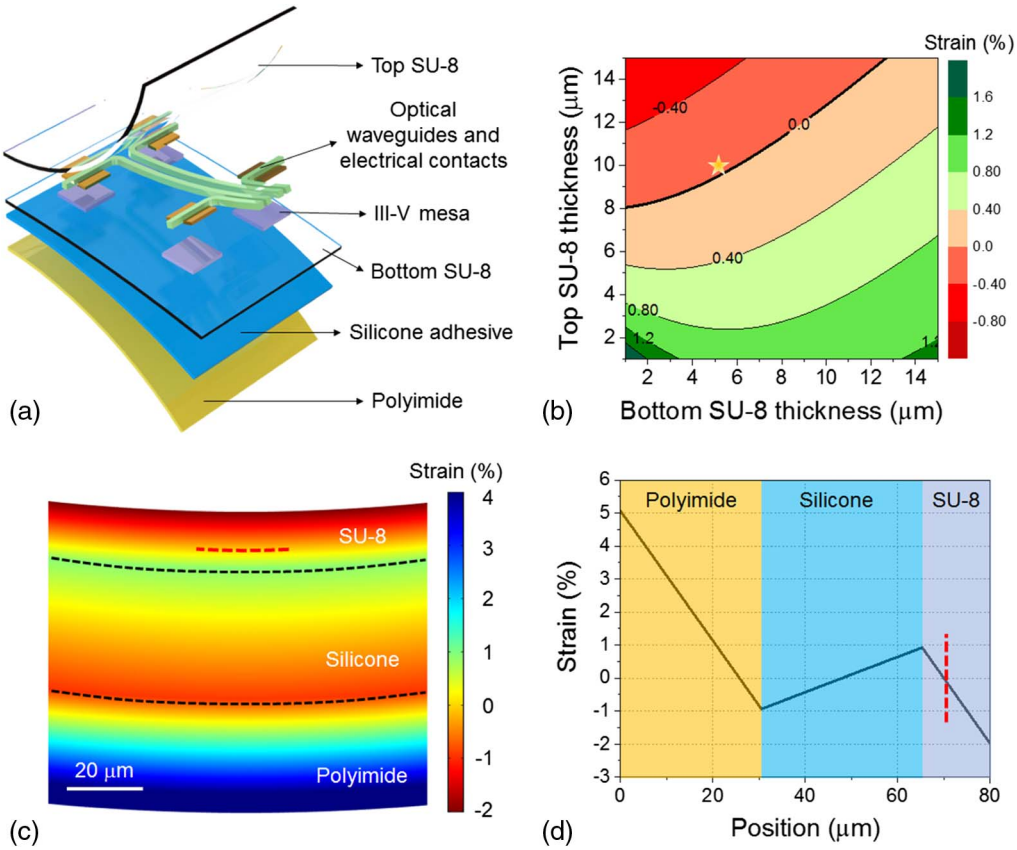

Fig. 2. (a) Laminated structure of the flexible detector; (b) local strain at the NM layer versus the thicknesses of top and bottom SU-8 claddings predicted using the MNA theory: the star represents the experimentally realized device structure; (c), (d) strain distribution in the fabricated device computed using FEM: the red dashed lines mark the position of the NM layer.

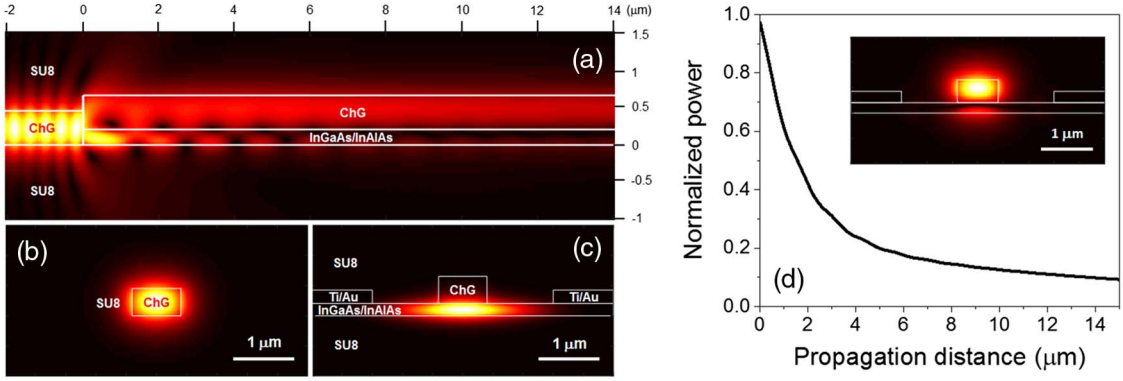

Fig. 3. (a) Side-view optical intensity distribution in the waveguide-coupled detector structure simulated using FDTD: the optical input is launched from the ChG waveguide on the left-hand-side; (b), (c) optical modal profiles in (b) the input ChG waveguide; and (c) the detector mesa with a loaded waveguide strip; (d) guided optical power flux in the hybrid ChG-detector mesa waveguide (normalized to input power) versus propagation distance along the structure; inset portrays the profile of the odd supermode, which is primarily confined in the ChG strip.

input) along the detector mesa. The rapid decrease within the first 5 μm is attributed to strong attenuation of the NM supermode, which has a large modal absorption coefficient of 2.6 dB/μm. In contrast, the ChG waveguide supermode only weakly interacts with the NM and exhibits a much smaller modal absorption coefficient of 0.25 dB/μm. As a result, light coupled into the ChG waveguide supermode is not fully absorbed by the detector, which accounts for the long tail in Fig. 3(d).

The fabricated devices were characterized using a home-built setup illustrated in Fig. 4. Light from an external cavity tunable laser (LUNA Technologies OVA-5000) was coupled into the device under test (DUT) either via grating couplers or through

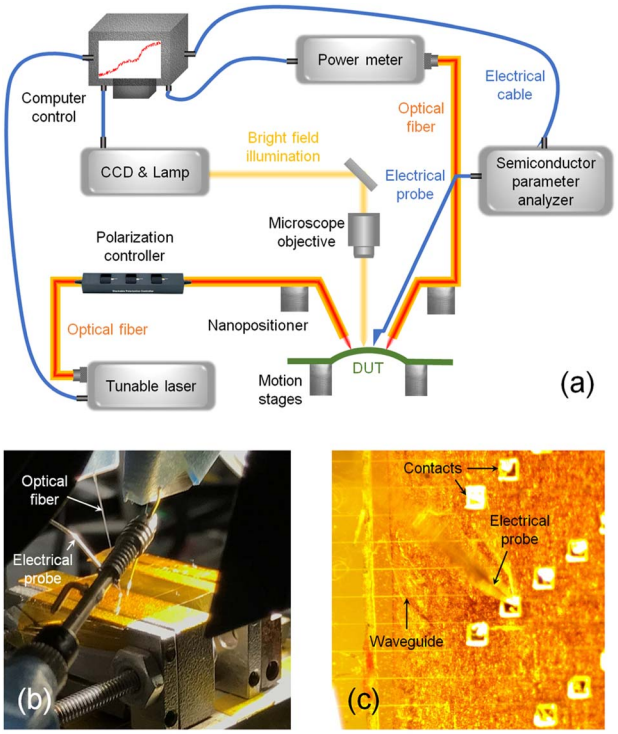

Fig. 4. (a) Schematic diagram of the device characterization setup; (b) photo of a flexible detector sample during the measurement; (c) top-view micrograph of a sample under test.

fiber end fire coupling. For most optical tests, the grating coupling scheme was used, with the only exception being the spectral response measurement [Fig. 6(d)] since the grating couplers only operate over a narrow wavelength range. A second set of devices with cleaved edge coupling facets (but otherwise identical) were prepared specifically for the spectral response measurement. The samples were mounted on a pair of linear motion stages such that they can be deformed *in situ* during optoelectronic characterizations. Bending radii of the DUT were extracted from side-view optical images [Fig. 6(a)] using the image processing software ImageJ.

To quantify the dynamic response of the detector, laser light at 1530 nm wavelength was first modulated by an electro-optic modulator (Lucent model X2623Y) driven by a network analyzer (Keysight Technologies E5061B). The modulated signal was subsequently amplified by an erbium-doped fiber amplifier before coupling into the detector. The photocurrent signal was transmitted through a G-S microwave probe (Cascade Microtech, Inc.) to the network analyzer to extract the scattering parameter S_{21}. Loss and frequency roll-off of the modulator were calibrated in the bandwidth calculation.

3. RESULTS AND DISCUSSION

Figures 5(a) and 5(b) show the measured dark and photo currents of the device. In Fig. 5(b) and our subsequent discussions, the optical power values are quoted as guided power in the waveguide estimated based on experimentally extracted coupling losses. Clear rectification behavior is observed in Fig. 5(a) with a low dark current of approximately 170 pA at 5 V bias, signaling that the InGaAs absorber layer and the InAlAs Schottky barrier enhancement layer maintain high quality after substrate removal. The photocurrent at 5 V bias was measured using a lock-in amplifier at 30 kHz chopping frequency and is plotted as a function of optical power in Fig. 5(c). The device exhibits a linear response from the lowest optical power that we can reliably calibrate in our experiment (40 pW) up to 0.4 mW (beyond which deviations from the linear response curve become pronounced), indicating a large linear dynamic range (LDR) in excess of 70 dB. The responsivity within the range is 0.35 A/W, corresponding to an external quantum efficiency of 28%. Figure 5(d) shows the measured frequency response of the device normalized to its static

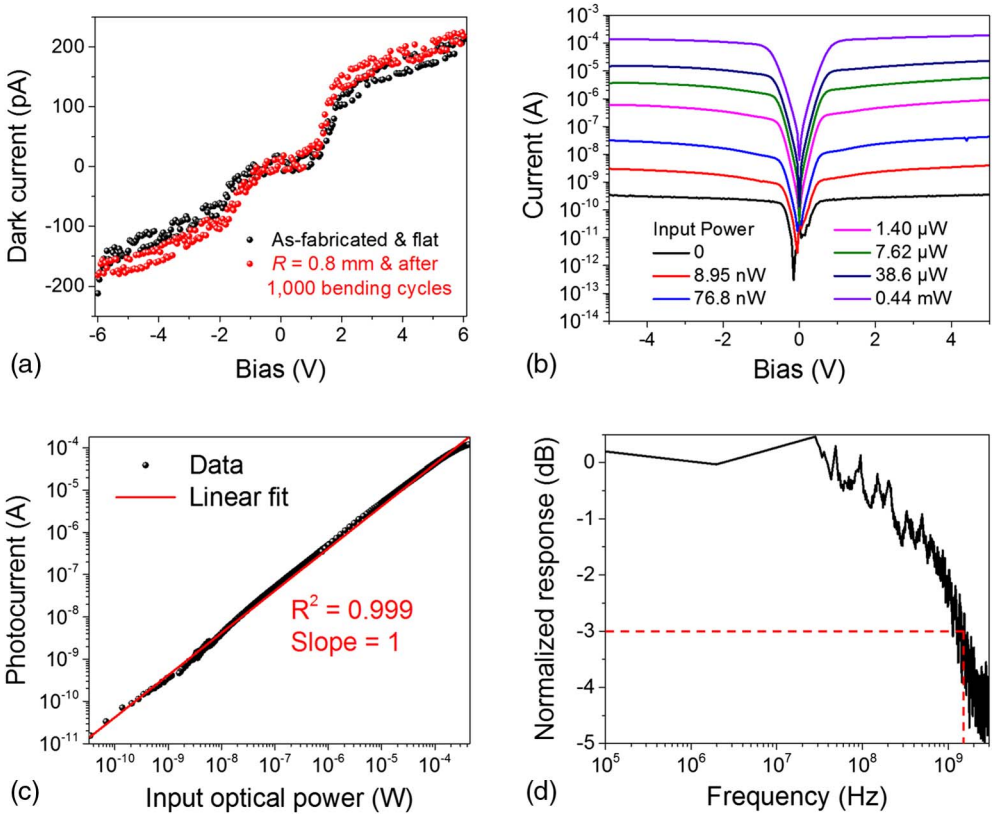

Fig. 5. (a) Dark current of the device measured: (black) in a flat state and (red) when bent to 0.8 mm radius and after 1000 bending cycles; (b) I–V responses of the detector at different input optical power levels; (c) double logarithm plot showing the linear dynamic range of the device; (d) dynamic response of the detector. The optical power values are quoted as guided power in the waveguide estimated based on experimentally extracted coupling losses.

responsivity, from which a 3-dB bandwidth of 1.4 GHz is inferred at 5 V bias. As is evident from Supplement 1 (Table S1), both the LDR and speed of our device represent major improvements over the state-of-the-art of flexible detectors.

To understand the factors limiting the device bandwidth, we estimated the resistive-capacitive (RC) delay time constant and carrier transit time. The waveguide-integrated geometry prompts a small detector footprint with an estimated device capacitance of 3.5 fF. With a 50-Ohm load used in our measurement, the RC-limited bandwidth amounts to 9.1 THz, which assures that the device bandwidth is not bound by RC delay. On the other hand, assuming a hole drift velocity of 1.4×10^4 m/s based on data quoted for bulk $In_{0.53}Ga_{0.47}As$ [54] yields a transit-time-limited bandwidth of 2.1 GHz, close to the measurement result of 1.4 GHz. The minor discrepancy likely arises from reduced carrier drift velocity in the NM compared to bulk semiconductors.

To evaluate the detector noise characteristics, we consider both dark-current shot noise and Johnson noise, while $1/f$ noise is discounted given the large 3-dB bandwidth of the detector. The respective noise power spectral densities are calculated according to [55]

$$S_s = 2qI_d \text{ (shot noise)}, \tag{1}$$

$$S_J = \frac{4k_BT}{R} \text{ (Johnson noise)}, \tag{2}$$

where q, I_d, k_B, T, and R denote electron charge, detector dark current, the Boltzmann constant, temperature, and shunt resistance, respectively. The total noise is the sum of both noise components. SNR performance of the detector is quantified through the noise equivalent power (NEP),

$$\text{NEP} = \frac{\sqrt{S_s + S_J}}{R_I}, \tag{3}$$

where R_I is the photocurrent responsivity of the detector. We note that NEP, rather than specific detectivity (D^*), forms the most appropriate figure of merit for waveguide-integrated photodetectors. This is because unlike their free-space counterparts, the dependence of SNR on square root detector area does not apply to waveguide-integrated detectors. Our analysis reveals that the detector exhibits a room-temperature NEP of 0.02 $\text{pW} \cdot \text{Hz}^{1/2}$, primarily limited by dark-current shot noise. This NEP figure represents, to the best of our knowledge, the lowest value reported for flexible detectors in the telecommunication wavelength range. We also fabricated reference detectors on a rigid substrate with an otherwise identical structure, and no measurable difference in NEP was observed in the reference devices, indicating that the flexible substrate integration process does not adversely impact the detector SNR.

We further show that the exceptional optoelectronic performance metrics of the detector are maintained even under severe mechanical deformation. Figure 5(a), 6(b), and 6(c), respectively, compare the detectors' dark current, responsivity and spectral response in their nondeformed and bent states. In the latter case, the results were taken when the device was bent to a radius of

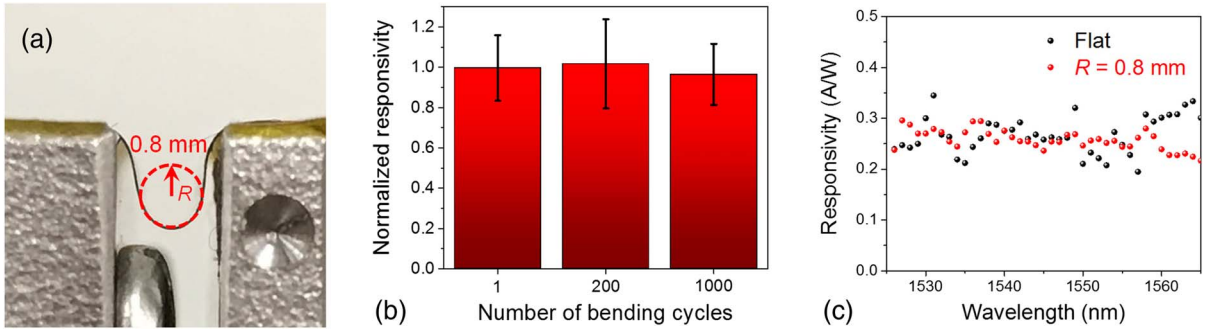

Fig. 6. (a) Side-view of the device bent to a radius of $R = 0.8$ mm; (b) responsivity of the detector measured at 0.8 mm bending radius and 1530 nm wavelength, after multiple bending cycles at $R = 0.8$ mm: the data are normalized to the detector responsivity in its as-fabricated, flat state and the error bars correspond to standard deviations over measurements taken on three devices; (c) spectral response of a flexible detector across the C-band measured at its nondeformed and bent states: note that the spectral measurement is taken using the edge coupling method and on a different device (albeit with a nominally identical device design).

0.8 mm. The results validate that the detector performance is unaffected by large bending down to sub-millimeter radius, a feat which was not accomplished in previous NM photodetector devices. Figures 5(a) and 6(b) also show that the device's dark current and responsivity remain unchanged after 1000 bending cycles at 0.8 mm radius. Such unprecedented mechanical ruggedness is attributed to the MNA mechanical design, which effectively suppresses strains at the NM during bending and thereby enhances material robustness.

4. CONCLUSION

In this paper, we demonstrated a flexible photodetector simultaneously achieving an NEP of 0.02 pW · $Hz^{1/2}$ at the telecommunication C-band, a LDR of over 70 dB, and a 3-dB bandwidth of 1.4 GHz, all of which set new records for flexible detectors. The significant improvements of SNR and speed over state-of-the-art detectors are made possible by a waveguide-integrated architecture that enhances light–matter interactions while maintaining a small device footprint. The waveguide-integrated detector uses chalcogenide glass as the monolithically integrated passive waveguide material and semiconductor NM as the active optoelectronic building block to combine the best of both worlds: the amorphous, low-temperature-processed ChG simplifies the integration process, whereas the pristine semiconductor material quality of single-crystalline NMs enables high speed and low noise.

In addition to its exceptional optical performance, our device also substantially outperforms previous NM devices in terms of mechanical robustness, leveraging a multi-neutral-axis configurational design. We show that the device can withstand 1000 bending cycles at 0.8 mm radius without measurable deterioration. The outstanding optoelectronic and mechanical performance of our device potentially pave the path towards many applications ranging from epidermal sensing to high-speed optical communications.

Both the device integration process and the MNA mechanical design are applicable to a wide array of flexible optoelectronic devices, such as optical modulators and light sources, which ultimately enables a fully integrated and flexible photonic integrated circuit.

Funding. National Science Foundation (NSF) (1453218, 1506605); U.S. Department of Energy (DOE) (DE-SC0001088).

Acknowledgment. The authors gratefully thank Lionel C. Kimerling and Anu Agarwal for providing access to device measurement facilities; Qingyang Du, Derek Kita, and Kurt Broderick for assistance with device processing and characterization; and Mark Mondol for technical support with electron beam lithography. The authors also acknowledge fabrication facility support by the MIT Microsystems Technology Laboratories and the Harvard University Center for Nanoscale Systems. R. J. S. was supported by the Center for Excitonics, an Energy Frontier Research Center funded by the U.S. Department of Energy, Office of Science, Office of Basic Energy Sciences.

See Supplement 1 for supporting content.

†These authors contributed equally to this work.

REFERENCES

1. E. Bosman, G. Van Steenberge, B. Van Hoe, J. Missinne, J. Vanfleteren, and P. Van Daele, "Highly reliable flexible active optical links," IEEE Photon. Technol. Lett. **22**, 287–289 (2010).
2. R. Dangel, F. Horst, D. Jubin, N. Meier, J. Weiss, B. J. Offrein, B. W. Swatowski, C. M. Amb, D. J. DeShazer, and W. K. Weidner, "Development of versatile polymer waveguide flex technology for use in optical interconnects," J. Lightwave Technol. **31**, 3915–3926 (2013).
3. L. Li, Y. Zou, H. Lin, J. Hu, X. Sun, N.-N. Feng, S. Danto, K. Richardson, T. Gu, and M. Haney, "A fully-integrated flexible photonic platform for chip-to-chip optical interconnects," J. Lightwave Technol. **31**, 4080–4086 (2013).
4. J. Missinne, E. Bosman, B. Van Hoe, G. Van Steenberge, S. Kalathimekkad, P. Van Daele, and J. Vanfleteren, "Flexible shear sensor based on embedded optoelectronic components," IEEE Photon. Technol. Lett. **23**, 771–773 (2011).
5. L. Fan, L. T. Varghese, Y. Xuan, J. Wang, B. Niu, and M. Qi, "Direct fabrication of silicon photonic devices on a flexible platform and its application for strain sensing," Opt. Express **20**, 20564–20575 (2012).
6. S. Yun, S. Park, B. Park, Y. Kim, S. K. Park, S. Nam, and K. U. Kyung, "Polymer-waveguide-based flexible tactile sensor array for dynamic response," Adv. Mater. **26**, 4474–4480 (2014).
7. H. Zhao, K. O'Brien, S. Li, and R. F. Shepherd, "Optoelectronically innervated soft prosthetic hand via stretchable optical waveguides," Science Robotics **1**, eaai7529 (2016).

8. T. Yokota, P. Zalar, M. Kaltenbrunner, H. Jinno, N. Matsuhisa, H. Kitanosako, Y. Tachibana, W. Yukita, M. Koizumi, and T. Someya, "Ultraflexible organic photonic skin," Sci. Adv. **2**, e1501856 (2016).
9. J. Kim, G. A. Salvatore, H. Araki, A. M. Chiarelli, Z. Xie, A. Banks, X. Sheng, Y. Liu, J. W. Lee, and K.-I. Jang, "Battery-free, stretchable optoelectronic systems for wireless optical characterization of the skin," Sci. Adv. **2**, e1600418 (2016).
10. S. Nizamoglu, M. C. Gather, M. Humar, M. Choi, S. Kim, K. S. Kim, S. K. Hahn, G. Scarcelli, M. Randolph, and R. W. Redmond, "Bioabsorbable polymer optical waveguides for deep-tissue photomedicine," Nat. Commun. **7**10374 (2016).
11. M. Humar, S. J. Kwok, M. Choi, A. K. Yetisen, S. Cho, and S.-H. Yun, "Toward biomaterial-based implantable photonic devices," Nanophotonics **6**, 414–434 (2017).
12. M. Choi, J. W. Choi, S. Kim, S. Nizamoglu, S. K. Hahn, and S. H. Yun, "Light-guiding hydrogels for cell-based sensing and optogenetic synthesis in vivo," Nat. Photonics **7**, 987–994 (2013).
13. Y. Zou, L. Moreel, H. Lin, J. Zhou, L. Li, S. Danto, J. D. Musgraves, E. Koontz, K. Richardson, and K. D. Dobson, "Solution processing and resist-free nanoimprint fabrication of thin film chalcogenide glass devices: inorganic-organic hybrid photonic integration," Adv. Opt. Mater. **2**, 759–764 (2014).
14. C. L. Yu, H. Kim, N. de Leon, I. W. Frank, J. T. Robinson, M. McCutcheon, M. Liu, M. D. Lukin, M. Loncar, and H. Park, "Stretchable photonic crystal cavity with wide frequency tunability," Nano Lett. **13**, 248–252 (2012).
15. Y. Zou, D. N. Zhang, H. T. Lin, L. Li, L. Moreel, J. Zhou, Q. Y. Du, O. Ogbuu, S. Danto, J. D. Musgraves, K. Richardson, K. D. Dobson, R. Birkmire, and J. J. Hu, "High-performance, high-index-contrast chalcogenide glass photonics on silicon and unconventional non-planar substrates," Adv. Opt. Mater. **2**, 478–486 (2014).
16. S. Aikio, J. Hiltunen, J. Hiitola-Keinänen, M. Hiltunen, V. Kontturi, S. Siitonen, J. Puustinen, and P. Karioja, "Disposable photonic integrated circuits for evanescent wave sensors by ultra-high volume roll-to-roll method," Opt. Express **24**, 2527–2541 (2016).
17. S. Aikio, M. Zeilinger, J. Hiltunen, L. Hakalahti, J. Hiitola-Keinänen, M. Hiltunen, V. Kontturi, S. Siitonen, J. Puustinen, and P. Lieberzeit, "Disposable (bio) chemical integrated optical waveguide sensors implemented on roll-to-roll produced platforms," RSC Adv. **6**, 50414–50422 (2016).
18. R. Bruck, P. Muellner, N. Kataeva, A. Koeck, S. Trassl, V. Rinnerbauer, K. Schmidegg, and R. Hainberger, "Flexible thin-film polymer waveguides fabricated in an industrial roll-to-roll process," Appl. Opt. **52**, 4510–4514 (2013).
19. H. J. Kang, T. Kim, and M. Y. Jeong, "PLC devices fabricated on flexible plastic substrate by roll-to-roll imprint lithography," J. Microelectron. Electron. Packag. **22**, 25–29 (2015).
20. R. Eckstein, T. Rodlmeier, T. Glaser, S. Valouch, R. Mauer, U. Lemmer, and G. Hernandez-Sosa, "Aerosol-jet printed flexible organic photodiodes: semi-transparent, color neutral, and highly efficient," Adv. Electron. Mater. **1**, 1500101 (2015).
21. G. H. Gelinck, A. Kumar, D. Moet, J. L. van der Steen, U. Shafique, P. E. Malinowski, K. Myny, B. P. Rand, M. Simon, W. Rutten, A. Douglas, J. Jorritsma, P. Heremans, and R. Andriessen, "X-ray imager using solution processed organic transistor arrays and bulk heterojunction photodiodes on thin, flexible plastic substrate," Org. Electron. **14**, 2602–2609 (2013).
22. H. Kong, J. Sinha, D. Hoeft, S. B. Kirschner, D. H. Reich, and H. E. Katz, "Solution processable organic p-n junction bilayer vertical photodiodes," Org. Electron. **14**, 703–710 (2013).
23. T. N. Ng, W. S. Wong, M. L. Chabinyc, S. Sambandan, and R. A. Street, "Flexible image sensor array with bulk heterojunction organic photodiode," Appl. Phys. Lett. **92**, 213303 (2008).
24. S. Zhang, L. Cai, T. Wang, J. Miao, N. Sepulveda, and C. Wang, "Fully printed flexible carbon nanotube photodetectors," Appl. Phys. Lett. **110**123105 (2017).
25. S. Lim, D. S. Um, M. Ha, Q. P. Zhang, Y. Lee, Y. J. Lin, Z. Y. Fan, and H. Ko, "Broadband omnidirectional light detection in flexible and hierarchical ZnO/Si heterojunction photodiodes," Nano Res. **10**, 22–36 (2017).
26. X. M. Xie and G. Z. Shen, "Single-crystalline In2S3 nanowire-based flexible visible-light photodetectors with an ultra-high photoresponse," Nanoscale **7**, 5046–5052 (2015).
27. G. Yu, Z. Liu, X. M. Xie, X. Ouyang, and G. Z. Shen, "Flexible photodetectors with single-crystalline GaTe nanowires," J. Mater. Chem. C **2**, 6104–6110 (2014).
28. G. Chen, B. Liang, Z. Liu, G. Yu, X. M. Xie, T. Luo, Z. Xie, D. Chen, M. Q. Zhu, and G. Z. Shen, "High performance rigid and flexible visible-light photodetectors based on aligned X(In, Ga)P nanowire arrays," J. Mater. Chem. C **2**, 1270–1277 (2014).
29. Z. Liu, G. Chen, B. Liang, G. Yu, H. T. Huang, D. Chen, and G. Z. Shen, "Fabrication of high-quality ZnTe nanowires toward high-performance rigid/flexible visible-light photodetectors," Opt. Express **21**, 7799–7810 (2013).
30. K. Heo, H. Lee, Y. Park, J. Park, H. J. Lim, D. Yoon, C. Lee, M. Kim, H. Cheong, J. Park, J. Jian, and S. Hong, "Aligned networks of cadmium sulfide nanowires for highly flexible photodetectors with improved photoconductive responses," J. Mater. Chem. **22**, 2173–2179 (2012).
31. Z. Q. Zheng, T. M. Zhang, J. D. Yao, Y. Zhang, J. R. Xu, and G. W. Yang, "Flexible, transparent and ultra-broadband photodetector based on large-area WSe2 film for wearable devices," Nanotechnology **27**, 225501 (2016).
32. D. B. Velusamy, R. H. Kim, S. Cha, J. Huh, R. Khazaeinezhad, S. H. Kassani, G. Song, S. M. Cho, S. H. Cho, I. Hwang, J. Lee, K. Oh, H. Choi, and C. Park, "Flexible transition metal dichalcogenide nanosheets for band-selective photodetection," Nat. Commun. **6**, 8063 (2015).
33. D. B. Velusamy, M. A. Haque, M. R. Parida, F. Zhang, T. Wu, O. F. Mohammed, and H. N. Alshareef, "2D organic-inorganic hybrid thin films for flexible UV-visible photodetectors," Adv. Funct. Mater. **27**, 1605554 (2017).
34. K. K. Manga, J. Z. Wang, M. Lin, J. Zhang, M. Nesladek, V. Nalla, W. Ji, and K. P. Loh, "High-performance broadband photodetector using solution-processible PbSe-TiO2-graphene hybrids," Adv. Mater. **24**, 1697–1702 (2012).
35. S. Chen, C. Teng, M. Zhang, Y. Li, D. Xie, and G. Shi, "A flexible UV-Vis-NIR photodetector based on a perovskite/conjugated-polymer composite," Adv. Mater. **28**, 5969–5974 (2016).
36. J. B. Li, Y. L. Shen, Y. C. Liu, F. Shi, X. D. Ren, T. Q. Niu, K. Zhao, and S. Z. F. Liu, "Stable high-performance flexible photodetector based on upconversion nanoparticles/perovskite microarrays composite," ACS Appl. Mater. Interfaces **9**, 19176–19183 (2017).
37. W. Deng, X. J. Zhang, L. M. Huang, X. Z. Xu, L. Wang, J. C. Wang, Q. X. Shang, S. T. Lee, and J. S. Jie, "Aligned single-crystalline perovskite microwire arrays for high-performance flexible image sensors with long-term stability," Adv. Mater. **28**, 2201–2208 (2016).
38. X. Hu, X. D. Zhang, L. Liang, J. Bao, S. Li, W. L. Yang, and Y. Xie, "High-performance flexible broadband photodetector based on organolead halide perovskite," Adv. Funct. Mater. **24**, 7373–7380 (2014).
39. M. Kim, J. H. Seo, Z. F. Yu, W. D. Zhou, and Z. Q. Ma, "Flexible germanium nanomembrane metal-semiconductor-metal photodiodes," Appl. Phys. Lett. **109**, 051105 (2016).
40. D. J. Fan, K. Lee, and S. R. Forres, "Flexible thin-film InGaAs photodiode focal plane array," ACS Photon. **3**, 670–676 (2016).
41. J. H. Seo, K. Zhang, M. Kim, D. Y. Zhao, H. J. Yang, W. D. Zhou, and Z. Q. Ma, "Flexible phototransistors based on single-crystalline silicon nanomembranes," Adv. Opt. Mater. **4**, 120–125 (2016).
42. W. Q. Yang, H. J. Yang, G. X. Qin, Z. Q. Ma, J. Berggren, M. Hammar, R. Soref, and W. D. Zhou, "Large-area InP-based crystalline nanomembrane flexible photodetectors," Appl. Phys. Lett. **96**, 121107 (2010).
43. H. C. Yuan, J. H. Shin, G. X. Qin, L. Sun, P. Bhattacharya, M. G. Lagally, G. K. Celler, and Z. Q. Ma, "Flexible photodetectors on plastic substrates by use of printing transferred single-crystal germanium membranes," Appl. Phys. Lett. **94**, 013102 (2009).
44. L. Li, H. Lin, S. Qiao, Y. Zou, S. Danto, K. Richardson, J. D. Musgraves, N. Lu, and J. Hu, "Integrated flexible chalcogenide glass photonic devices," Nat. Photonics **8**, 643–649 (2014).
45. L. Li, P. Zhang, W.-M. Wang, H. Lin, A. B. Zerdoum, S. J. Geiger, Y. Liu, N. Xiao, Y. Zou, and O. Ogbuu, "Foldable and cytocompatible sol-gel TiO_2 Photonics," Sci. Rep. **5**, 13832 (2015).
46. Y. Shi, J. A. Rogers, C. Gao, and Y. Huang, "Multiple neutral axes in bending of a multiple-layer beam with extremely different elastic properties," J. Appl. Mech. **81**, 114501 (2014).

47. D. Ahn, C.-Y. Hong, J. Liu, W. Giziewicz, M. Beals, L. C. Kimerling, J. Michel, J. Chen, and F. X. Kärtner, "High performance, waveguide integrated Ge photodetectors," Opt. Express **15**, 3916–3921 (2007).
48. J. Missinne, S. Kalathimekkad, B. Van Hoe, E. Bosman, J. Vanfleteren, and G. Van Steenberge, "Stretchable optical waveguides," Opt. Express **22**, 4168–4179 (2014).
49. C. Choi, L. Lin, Y. Liu, J. Choi, L. Wang, D. Haas, J. Magera, and R. T. Chen, "Flexible optical waveguide film fabrications and optoelectronic devices integration for fully embedded board-level optical interconnects," J. Lightwave Technol. **22**, 2168–2176 (2004).
50. D. Guidotti, J. Yu, M. Blaser, V. Grundlehner, and G.-K. Chang, "Edge viewing photodetectors for strictly in-plane lightwave circuit integration and flexible optical interconnects," in *56th Electronic Components and Technology Conference* (IEEE, 2006), p. 7.
51. H. Zheng, J. Ding, L. Zhang, S. An, H. Lin, B. Zheng, Q. Du, G. Yin, J. Michon, and Y. Zhang, "Ultra-thin, high-efficiency mid-infrared transmissive Huygens meta-optics," arXiv:1707.00760 (2017).
52. J. Hu, V. Tarasov, A. Agarwal, L. Kimerling, N. Carlie, L. Petit, and K. Richardson, "Fabrication and testing of planar chalcogenide waveguide integrated microfluidic sensor," Opt. Express **15**, 2307–2314 (2007).
53. J. J. Hu, V. Tarasov, N. Carlie, N. N. Feng, L. Petit, A. Agarwal, K. Richardson, and L. Kimerling, "Si-CMOS-compatible lift-off fabrication of low-loss planar chalcogenide waveguides," Opt. Express **15**, 11798–11807 (2007).
54. K. Brennan, "Theory of the steady-state hole drift velocity in InGaAs," Appl. Phys. Lett. **51**, 995–997 (1987).
55. E. L. Dereniak and G. D. Boreman, *Infrared Detectors and Systems* (Wiley, 1996).